ANALYSIS OF TEMPERATURE DISTRIBUTIONS IN A GERMICIDAL CHAMBER SUPPORTED BY LIGHT-ILLUMINATED GOLD NANORODS USING CFD-EQUATIONS AND A THERMAL CAMERA

Piotr Radomski[1*], Dominik Kreft[1], María C. Nevárez Martínez[2,3], Aimad Koulali[1], Iuliia Mukha[4,5], Luciano De Sio[6], Paweł Ziółkowski[1] and Dariusz Mikielewicz[1]

[1]Gdansk University of Technology, Faculty of Mechanical Engineering and Ship Technology, Gdansk, Pomerania, Poland

[2]University of Gdansk, Faculty of Chemistry, Department of Environmental Technology, Gdansk, Pomerania, Poland

[3]Center for Integrated Nanotechnologies, Los Alamos National Laboratory, Los Alamos, 87545, New Mexico, United States of America

[4]National Center for Tumor Diseases (NCT/UCC), Dresden, Saxony, Germany

[5]Chuiko Institute of Surface Chemistry, The National Academy of Science of Ukraine, Kyiv, Kyiv Oblast, Ukraine

[6]Sapienza University of Rome, Department of Medico-Surgical Sciences and Biotechnologies, Latina, Lazio, Italy

*Corresponding Author: piotr.radomski@pg.edu.pl

ABSTRACT

Since the COVID-19 pandemic, protection against pathogenic germs and surface disinfection have become critical issues. Most effective bacteria/virus inactivation methods are either power-consuming or require using caustic chemical substances. Herein, thermal inactivation appears to be an affordable and effective technique as long as high temperatures are reached quickly and long-termly maintained. Therefore, the preparation of a chamber that accomplishes this purpose has been envisioned, designed and manufactured, allowing significant germ inactivation and offering an effective tool for water purification stations. In this regard, this work proposes applying 16-16-65-nm laser-illuminated gold nanorods (AuNRs) as a non-standard heat source, which can produce the generated heat inside a considered volume. Consequently, the locations of AuNRs deposited on glass platforms, stuck on the internal or external chamber's walls, from two sides, were investigated to intensify the heat transfer processes upon the entire chamber. To verify the efficiency of the energy conversion from light to heat, spectroscopy techniques and laser power meters were used. Similarly, temperature fields at the illuminated platforms were solved using the Computational Fluid Dynamics (CFD) equations and two different theoretical models which adopt the Rayleigh approximation and consider the delivered heat flux with a fixed efficiency, respectively. The considered Models were verified using a calibrated and highly-resolved thermal camera. Upon 900-mW 808-nm laser illumination for 50 min, the temperature of the platforms increased by $\Delta T \approx 57.1$℃ and $\Delta T \approx 388.3$℃ for an unfocused and focused beam, respectively. However, the quickest heat diffusion process is visible when the AuNR platform is situated in the internal position of the chamber, offering $\Delta T \approx 39.4$℃ after 50 min of illumination.

Keywords: energy conversion, gold nanorods, bacterial disinfection, germicidal chamber, CFD

1 INTRODUCTION

For ages, civilizations have been exposed and been sensitive to diseases spread by germs, which infect animals and potable water. This usually contributes to severe illnesses and increases local epidemics, which is a challenge to overcome in poor countries. Although global diseases happen rarely, the epidemic outbreaks are not usually nipped in the bud, and therefore still not fully controlled, which usually contributes to global severe situations. Thanks to mass media, the last one, COVID-19 pandemics,

brought bigger social awareness of germ protection and disinfection, and therefore the necessity of bacteria and viruses elimination has become an everyday habit for the majority of people.

Research suggests that conventional methods such as chemical disinfectants and filtration systems, while effective, often do not provide a rapid response to severe microbial epidemics. Thermal inactivation has emerged as a powerful alternative, due to its effectiveness across a wide range of microbial risks. For example, bacteria can generally be inactivated at around 65°C (Wen *et al.*, 2022), but more resistant viruses, such as SARS-CoV-2, require temperatures approaching 95°C (Hemati *et al.*, 2021). However, conventional heating methods are energy-intensive and slow; thus, pointing to the lack of fast and efficient heat application technologies (Klein *et al.*, 2023). Innovative solutions, such as the use of nanotechnologies, have been explored in recent publications (Zaccagnini *et al.*, 2023). Gold nanorods (AuNRs), for example, have been studied for their unique ability to efficiently convert light into heat when integrated into a biocompatible platform. Likewise, AuNRs have been applied for cancer therapy or imaging using near- and short-wave infrared lasers (Wang *et al.*, 2024; Lingg *et al.*, 2023).

Consequently, gold nanorods (AuNRs) have been selected in this work due to their effectiveness in energy conversion. AuNRs are highly attractive photothermal conversion agents owing to their absorption and scattering in the visible and near infrared ranges. They offer high photothermal conversion efficiency, tunability of optical properties by controlling the synthesis conditions and relatively straightforward surface modification to achieve the biocompatibility. Moreover, AuNRs present two plasmon bands associated to absorption and scattering along their long and short axes (Link *et al.*, 2000; Liz-Marzán *et al.*, 2020; Murphy *et al.*, 2011). Recent studies (Shao *et al.*, 2022; Peng *et al.*, 2022) show that AuNRs can be effectively applied in both bacteria and virus deactivation.

Herein, 16-16-65-nm AuNRs, which are embedded in the electrically ungrounded platform, can achieve rapid temperature increases, converting the incoming light to heat with a high efficiency (even 70%), which is crucial for rapid microbial inactivation. Nonetheless, the challenges appear when accelerating heat diffusion on the entire chamber is considered in order to achieve uniform temperature distribution, which is not a trivial issue. On the first hand, electric-grounded platforms imply using low-thermal-conductivity materials, which provides slow heat transfer and high temperature increase at the same time. On the other hand, if metallic platforms were adopted, it would reduce the heating time, but the temperature would not be sufficient to inactivate the total amount of germs. Hence, the combination of low- and high-diffusive materials strongly affect the germ inactivation effectiveness, and the system. In the field of Computational Fluid Dynamics (CFD), numerous works have been conducted to analyze flow and heat transfer inside square and rectangular cavities, under 3D (Li *et al.*, 2024) and 2D assumptions (Ji *et al.*, 2024). Amongst the parameters which influence the flow and heat distribution, particularly, the intensity and location of the heat source (Zhan *et al.*, 2019) or the geometric shape of the chamber (El Moutaouakil *et al.*, 2021) have been studied.

The purpose of this work is to examine which location (position) of the AuNR platform would bring the highest and the quickest temperature increase with uniform distribution in a germicidal chamber which was designed to provide fast heat diffusion, like in the Qu *et al.*, 2023 paper. This could assist to optimize the construction where germs and microbes are to be inactivated effectively.

2 METHODOLOGY

2.1 Energy conversion by light-illuminated AuNR platforms

The energy conversion rate determines the total amount of energy which is directly responsible for the heat production. Nevertheless, it is indicated to distinguish the total efficiency, η_{TOT}, the photothermal efficiency, η_{PT}, and the absorbed part of irradiation which are related to each other. In a classical mode, the absorbance can be established by using the Lambert-Beer-Bourger law, as follows:

$$\mathbf{ABS} = -\log_{10}\frac{I_{\mathbb{T}}}{I_0} \cong -\log_{10}\left(\left(1-\mathbb{R}_{pl}\right)\cdot\left(\exp\left(-\left(\iota_{ph}\right)\cdot\left(\left(\sigma_{ext}\right)\right)\right)\right)\right) =$$

$$= -\log_{10}\left(\left(1-\mathbb{R}_{pl}\right)\cdot\left(\exp\left(-\left(d_s+2\cdot d_{CT}\right)\cdot\left(\xi\cdot\left(\eta_{PT}\cdot C_{ext}\right)\right)\right)\right)\right) \quad (1)$$

It is noteworthy to emphasize that $\mathbb{R}_{pl}$, η_{PT} and C_{ext} are truly functions of incident wavelength, λ, and the maximum efficiency can be easily shifted and adjusted for different nanoparticle's shapes and sizes, and moreover – for different working media and platform's materials. Therefore, the balance between an incoming light and nanorods' properties is a crucial issue to reach the plasmon resonance, which provides the greatest temperature increase. To establish the energy conversion rate in the simulations, two different approaches are compared and confronted with the experiments. The first model (Model I) specifies the energy conversion of gold nanorods from light into heat by the volume source term in the energy equation, according to Radomski's et al. (2021; 2023a;b) papers:

$$\mathcal{S}_e = \left(\xi\cdot\left(\eta_{PT}\cdot C_{ext}\right)\right)\cdot\frac{P_0}{\pi\cdot B^2}\cdot$$
$$\cdot\left(1-\mathbb{R}_{pl}\right)\cdot\left(1-\mathbb{R}_{Au}\right)\cdot(FF)\cdot\left(1-\exp\left(-\left(d_s+2\cdot d_{CT}\right)\cdot\left(\xi\cdot\left(\eta_{PT}\cdot C_{ext}\right)\right)\right)\right) \quad (2)$$

where the photothermal efficiency, η_{PT}, is described by Pelton and Bryant (2013) and Jiang *et al.*, (2013) models, as follows:

$$\eta_{PT} = \frac{C_{abs}(d_s,d_l,d_{CT},\boldsymbol{\varepsilon_{Au}},n_w,\lambda)}{C_{ext}(d_s,d_l,d_{CT},\boldsymbol{\varepsilon_{Au}},n_w,\lambda)}\cdot\frac{1}{1+\frac{P_0}{P_{sat}(\xi)}} = 1-\frac{C_{sca}(d_s,d_l,d_{CT},\boldsymbol{\varepsilon_{Au}},n_w,\lambda)}{C_{ext}(d_s,d_l,d_{CT},\boldsymbol{\varepsilon_{Au}},n_w,\lambda)}\cdot\frac{1}{1+\frac{P_0}{P_{sat}(\xi)}} \quad (3)$$

and the optical cross-sections, C_{ext}, C_{sca} and C_{abs}, are determined by the Rayleigh-Drude approximation (Bohren and Huffman, 1983; Radomski *et al*., 2024) following the double-layered ellipsoid shape. As may be realized, the power correction implies that the source of energy increasing reaching plateau as the power increase. The inversely relations, however, are visible for the correlation between the source of energy and saturated power, although both parameter flattens. Depending on the nanoparticles concentration, ξ, the saturation power is assumed empirically from SEM/TEM images and from experimental results (Zaccagnini *et al*., 2023), as follows:

$$P_{sat}(\xi) = 1.56 + 1.13\cdot 10^{-23}\cdot\xi \quad (4)$$

where the number of AuNRs per volume (concentration) is assumed empirically by:

$$\xi = \frac{2}{(d_s+2\cdot dCT+\phi)^2\cdot(d_l+2\cdot dCT+\phi)} \quad (5)$$

The second approach (Model II) assumes energy conversion as a heat flux, and describes the delivered heat by the total efficiency, according to the formula:

$$\eta_{TOT} = \frac{I_{abs}}{I_0} \cong \frac{P_{abs}}{P_0} =$$
$$= \left(1-\mathbb{R}_{pl}\right)\cdot\left(1-\mathbb{R}_{Au}\right)\cdot(FF)\cdot\left(1-\exp\left(-\left(d_s+2\cdot d_{CT}\right)\cdot\left(\xi\cdot\left(\eta_{PT}\cdot C_{ext}\right)\right)\right)\right) \quad (6)$$

where the fill factor, FF, is assumed as:

$$FF = \frac{(d_s+2\cdot d_{CT})\cdot(d_l+2\cdot d_{CT})}{(d_s+2\cdot d_{CT}+\phi)\cdot(d_l+2\cdot d_{CT}+\phi)} \quad (7)$$

Different techniques can be applied to examine the transmission part, like spectroscopy measurement or power metering. The first one allows to fix the reflected part to zero by calibration processes, and is

frequently presented in a logarithmic scale, whereas power metering takes the advantage of determining transmitted part, and hence the conversion efficiency, at each selected positions.

Moreover, Model I assumes a gaussian distribution in space regime, which is expressed by the formula:

$$P_0 \rightarrow P_{MAX} \cdot \exp\left(-2 \cdot \left(\frac{\vec{r}}{B}\right)^2\right) \tag{8}$$

where $\vec{r}$ is the radial coordinate from cylindrical system, and $\mathbb{D}_{sp}$ is the sample spot diameter.

On the other hand, model II averages the delivered heat in the whole round sample spot, yielding:

$$P_0 \rightarrow \frac{\int_{-\mathbb{D}_{sp}/2}^{\mathbb{D}_{sp}/2} \int_0^{2\pi} P_{MAX} \cdot \exp\left(-2 \cdot \left(\frac{r}{B}\right)^2\right) d\phi \, dr}{\pi \cdot \left(\frac{\mathbb{D}_{sp}}{2}\right)^2} \tag{9}$$

Table 1 specifies the AuNRs dimensions and the parameters required for the CFD calculations. Size and shape distributions of nanorods are assumed to have lorentzian and gaussian curves, respectively, where the error is associated with the curve's variance.

Table 1 Assumed AuNRs and laser parameters which enable calculation of temperature contours (Zaccagnini *et al*., 2023; Radomski *et al*., 2023a)

Parameter	**Symbol**	**Value**		**Unit**
AuNRs dimensions	d_s x d_s x d_l	(16.0 ± 3.0) x (16.0 ± 3.0) x (65.0 ± 9.0)		nm
Size of capping agent (CTAB)	d_{CT}	4.0		nm
Distance between nanoparticles	φ	1.3		nm
Nanoparticle number concentration	ξ	$(4.7 \pm 1.4) \cdot 10^{22}$		m^{-3}
Saturated power	P_{sat}	2.091		W
Incoming light power	P_0	0.900		W
Beam sizes	B	4.0 *or* 2.5		mm
Incident wavelengths (nm)	λ	640	808	nm
Refractive index of water	n_w	1.3331490	1.328084	-
Refractive index of air	n_{air}	1.000278	1.000279	-
Permittivity of gold	$\boldsymbol{\varepsilon_{Au}}$	$-12.183069 + 1.173409 \cdot \mathbb{i}$	$-24.873107 + 1.554937 \cdot \mathbb{i}$	-
Reflected part of light for platform	$\mathbb{R}_{Au}$	0.154347	0.284140	-
Refractive index of the capping agent	n_{CT}	1.524937	1.520564	-
Photothermal efficiency	η_{PT}	0.967319	0.856535	-
Reflected part of light for platform	$\mathbb{R}_{pl}$	0.0431885	0.0426189	-

2.2 Considered systems

A water-filled germicidal chamber has been designed so as to enable measurements both inside and outside the chamber. The chamber is made of aluminum PA6 alloy and polycarbonate (PC) glass from one side. Furthermore, to examine the heat transfer processes, three positions have been selected – inside the chamber at the PC glass wall (Pos 1), at the back (Pos 2) and at the side aluminum wall (Pos 3), respectively. AuNRs have been deposited on a thin 1-cm round borosilicate glass with an 8-mm diameter spot and dried at 70°C for 15 min. Figures 1 reveal these three positions of the platforms which

are sandwiched using two pieces of the glass separated by a AuNRs slab and a NOA-61 transparent glue to join pieces and to protect AuNRs against their extrication or spilling out (Figure 2).

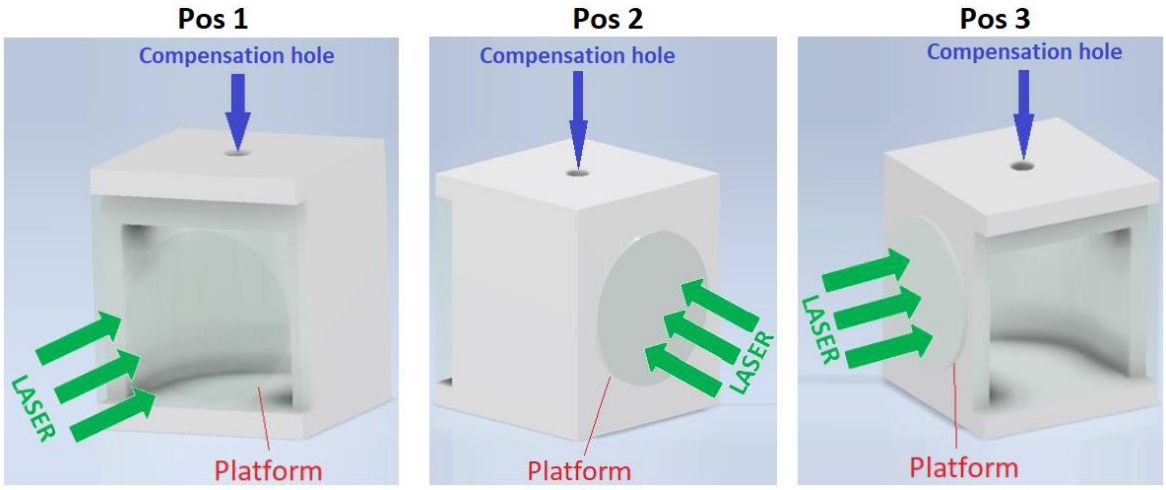

Figure 1: Scheme of the 1.3-cm manufactured germicidal chamber with the laser-illuminated platforms glued to PC glass and aluminum walls set at three key positions (Pos). Hole marked by blue color prevents against undesirable pressure destruction.

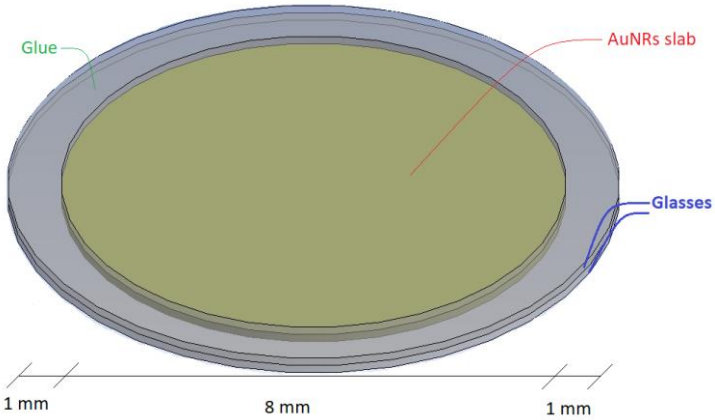

Figure 2: Scheme and dimensions of the sandwiched platform with a AuNRs slab

2.3 CFD numerical methods

To solve temperature distributions, the ANSYS software, v. 23.2, has been chosen. As a solution method COUPLED algorithm is selected with the second-order upwind schemes. Simulations concern solving computational-fluid-dynamics (CFD) equations, including mass conservation, momentum, energy, turbulence, and dissipation balance equations. The geometry of the chamber has been discretized to non-structural grids, whose mean size equals $L_{gg} = 80$ µm, and results have been extrapolated to the maximum numerical errors, 0.5% and 2.0% for temperature and velocity regimes, respectively.

The boundary conditions are fixed to mixed conditions, whereas initial conditions have been determined by using the calibrated weather station in the laboratory at $T_0 = 20^{\circ}\mathrm{C}$, $p_0 = 1009$ hPa, $H_0 = 35\%$. Necessary thermal properties of the applied materials are visible in Table 2, whereas Table 3 details mixed boundary conditions, including convection and radiation processes. With respect to CFD calculations, boundary conditions play a key role both in properly describing the physical phenomena occurring at the interface and in verifying the agreement of the model with experiment (Ziółkowski and Badur, 2018).

Table 2 Material properties used in this work (Zaccagnini *et al*., 2023; Radomski *et al*., 2021; URL 1)

Material	Property	Value	Unit
Aluminum PA6	Density, ρ	2,790.00	$kg \cdot m^{-3}$
	Specific heat capacity, c_p	873.00	$J \cdot kg^{-1} \cdot K^{-1}$
	Thermal conductivity coefficient, k	134.00	$W \cdot m^{-1} \cdot K^{-1}$
PC glass	Density, ρ	1,198.00	$kg \cdot m^{-3}$
	Specific heat capacity, c_p	1,199.00	$J \cdot kg^{-1} \cdot K^{-1}$
	Thermal conductivity coefficient, k	0.20512	$W \cdot m^{-1} \cdot K^{-1}$
Water	Density, ρ	998.20	$kg \cdot m^{-3}$
	Specific heat capacity, c_p	4,181.88	$J \cdot kg^{-1} \cdot K^{-1}$
	Thermal conductivity coefficient, k	0.60343	$W \cdot m^{-1} \cdot K^{-1}$
	Dynamic viscosity, μ	$9.8484 \cdot 10^{-3}$	$Pa \cdot s$
Borosilicate glass	Density, ρ	2,124.9	$kg \cdot m^{-3}$
	Specific heat capacity, c_p	779.74	$J \cdot kg^{-1} \cdot K^{-1}$
	Thermal conductivity coefficient, k	1.15	$W \cdot m^{-1} \cdot K^{-1}$
Air	Density, ρ	1.225	$kg \cdot m^{-3}$
	Specific heat capacity, c_p	1,006.43	$J \cdot kg^{-1} \cdot K^{-1}$
	Thermal conductivity coefficient, k	0.0242	$W \cdot m^{-1} \cdot K^{-1}$
	Dynamic viscosity, μ	$1.9 \cdot 10^{-5}$	$Pa \cdot s$
Glue	Density, ρ	1,290.00	$kg \cdot m^{-3}$
	Specific heat capacity, c_p	1,100.00	$J \cdot kg^{-1} \cdot K^{-1}$
	Thermal conductivity coefficient, k	0.50	$W \cdot m^{-1} \cdot K^{-1}$
	Dynamic viscosity, μ	0.30	$Pa \cdot s$
Gold	Density, ρ	19,320.00	$kg \cdot m^{-3}$
	Specific heat capacity, c_p	129.81	$J \cdot kg^{-1} \cdot K^{-1}$
	Thermal conductivity coefficient, k	317.00	$W \cdot m^{-1} \cdot K^{-1}$

Table 3 Details of the assumed boundary conditions (Siegel *et al*., 1972)

Material	Type of boundary conditions	Parameter	Unit
Aluminum PA6	Mixed	Heat transfer coefficient, h	$10.0\ W \cdot m^{-2} \cdot K^{-1}$
		Emissivity, ϵ	0.77
		Initial temperature, T_0	20^oC
PC glass	Mixed	Heat transfer coefficient, h	$10.0\ W \cdot m^{-2} \cdot K^{-1}$
		Emissivity, ϵ	0.92
		Temperature, T_0	20^oC
Glue	Mixed	Heat transfer coefficient, h	$5.0\ W \cdot m^{-2} \cdot K^{-1}$
		Emissivity, ϵ	0.93
		Initial temperature, T_0	20^oC
Borosili-cate glass	Mixed	Heat transfer coefficient, h	$13.6\ W \cdot m^{-2} \cdot K^{-1}$
		Emissivity, ϵ	0.957
		Initial temperature, T_0	20^oC

3 RESULTS

Figure 3 presents theoretical, achieved with the Models I and II, and experimental spectroscopy results (Spectrophotometer Thermo Fisher Scientific Evolution 220) calibrated to a water-filled cuvette. As may be noticed, two absorbance peaks appear at ~520 nm (green color) and ~835 nm, whereas the second one implies much higher energy conversion. Furthermore, Models are compared with experiments using laser power meter (Gentech 11MAESTRO with detector 11UP19K-15S-H5 from the Standa Ltd. company) which averages power from the reading area, performed in Model II. According

to the theoretical results for λ=640 nm and λ=808 nm, the total efficiency equals 0.42714 and 0.66061, respectively, which corresponds promisingly with the experimental data. The visible discrepancies are supposed to be explained by the temperature effects of the discussed thermo-optical properties, which has not been included in this work. Hence, the comparison satisfies the agreement between experimental and theoretical results, and the energy conversion is valid if the Rayleigh criterion, $\frac{\lambda}{2\pi} > d_l$, is not reached.

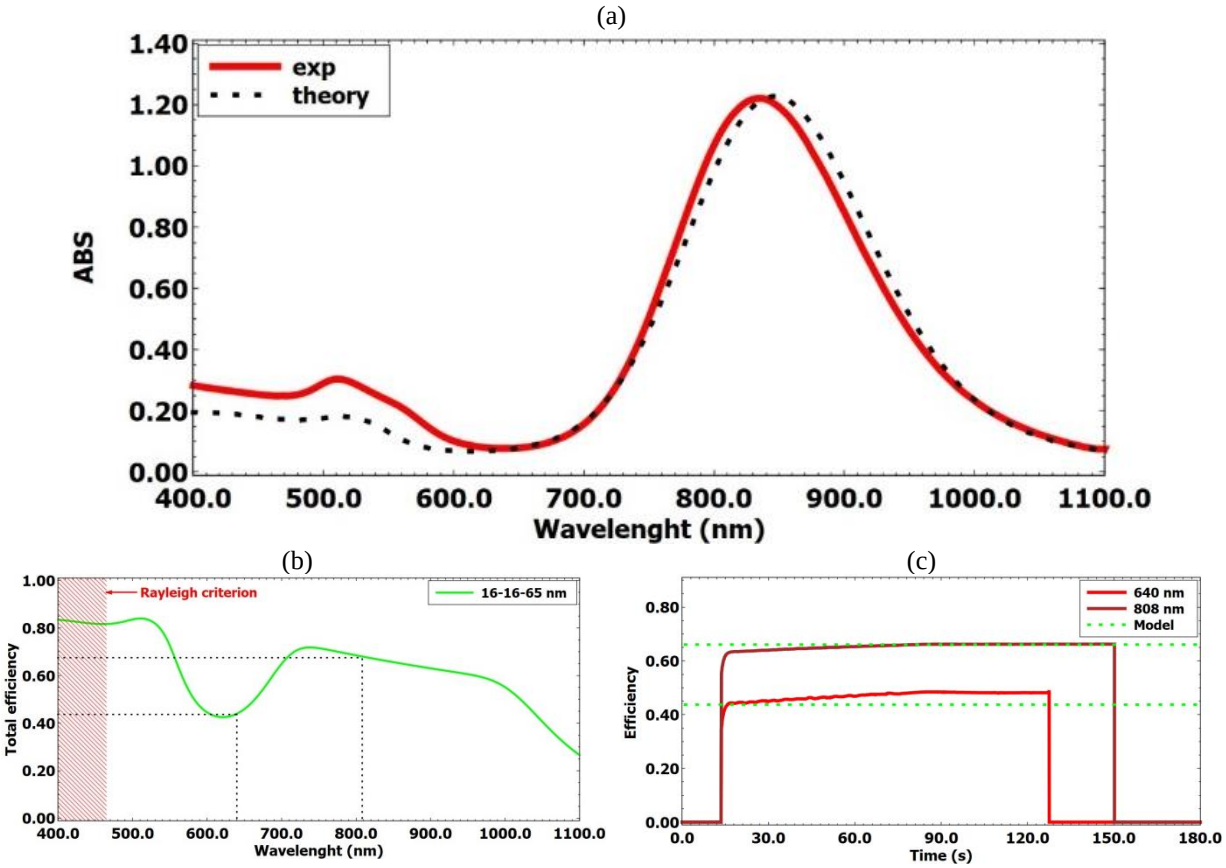

Figure 3: (a) Theoretical (Model I) and experimental results (exp) of gold nanorod platforms absorbance (**ABS**) over incident wavelength, λ; (b) theoretical results (Model II) of the energy conversion efficiency, η_{TOT}, over incident wavelength, λ; (c) laser power meter measurements of gold nanorod platforms presented in Figure 2.

Moreover, Figures 4 compare the steady-state temperature contours using the two presented models for the third location (Pos 3), which are also confronted with the InfiRay T600 thermal camera measurements. As may be noticed, experimental results present the temperature increase of $\Delta T_{\text{exp}} \approx 57.1$℃ after 30 minutes, which confirms the effectiveness and the potential of applying gold nanorods in this area. From the theoretical point of view, the Model I, where the temperature increases by $\Delta T_1 \approx 58.6$℃, appears to exhibit better agreement with experiments than the Model II, which provides $\Delta T_2 \approx 35.2$℃.

Nevertheless, due to the fact that the considered Models offer similar values of mean temperature in the fluid zone, it is presumed that averaging the energy conversion in the whole sample spot affects the visible discrepancies in the energy conversion rate and the maximum temperature, reaching a dozen Celsius degrees difference between these two models. Hence, both Models are expected to provide similar results as long as the spatial distribution of the beam would be included. However, the Model II requires less processing time. Therefore, its performance points out the necessity for calibration in spatial regime against empirical data to ensure reliability, especially in critical applications such as germicidal efficacy (Xu et al., 2003).

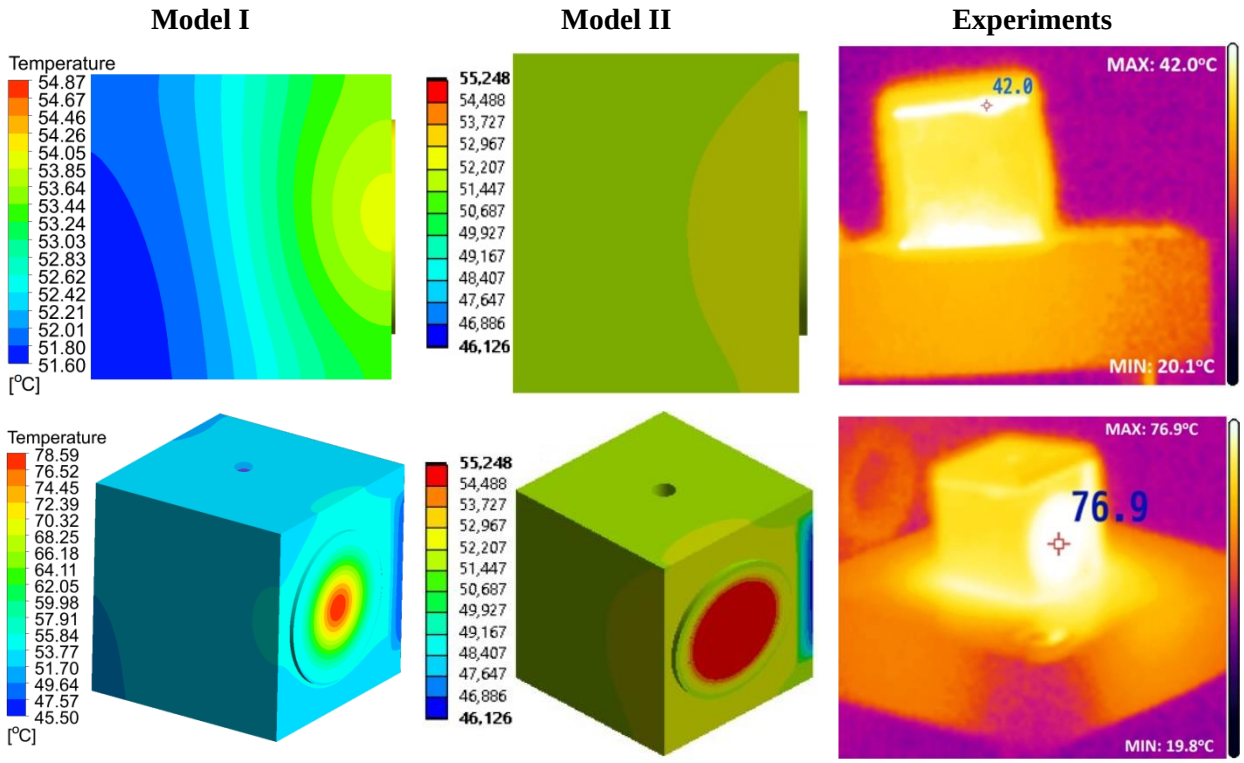

Figure 4: Side (up) and diagonal (down) views of the steady-state temperature distributions for the Pos 3 case from Model I (left), Model II (middle), and thermal camera results (right) after 20 min of illumination

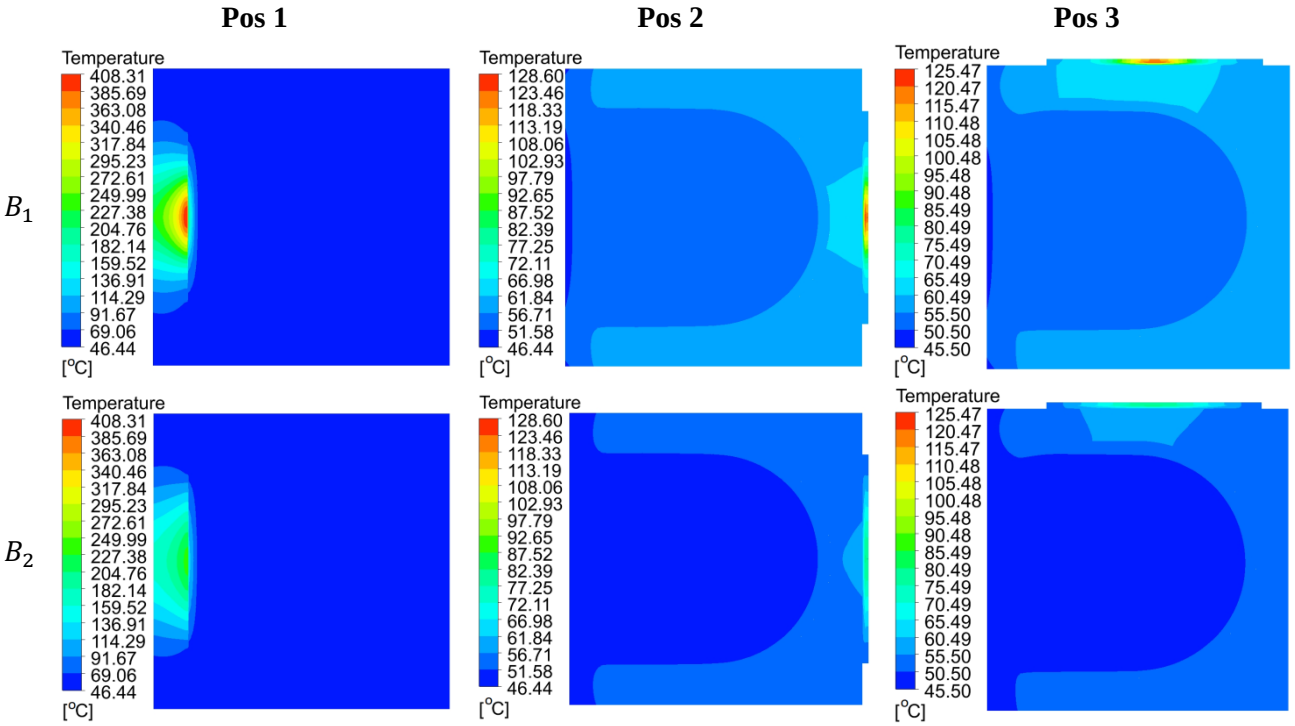

Figure 5: Steady-state temperature distributions of penetrated system for the three assumed platform positions, Pos 1 (left), Pos 2 (center), Pos 3 (right), and for two beam sizes (B_1=2.5 mm (up) and B_2=4.0 mm (down))

Consequently, on the basis of the energy conversion results, transient temperature contours of the germicidal chamber for the three platform positions are investigated for the Model I. Figures 5 reveal the steady-state results for two beam sizes, $B_1 = 2.5$ mm and $B_2 = 4.0$ mm, when mean temperature

values have been flattened and velocities have stagnated. Likewise, Figure 6 reveals transient results of the time responses of the average magnitude of velocity and the average temperature in the fluidic zone for each location and two beam sizes.

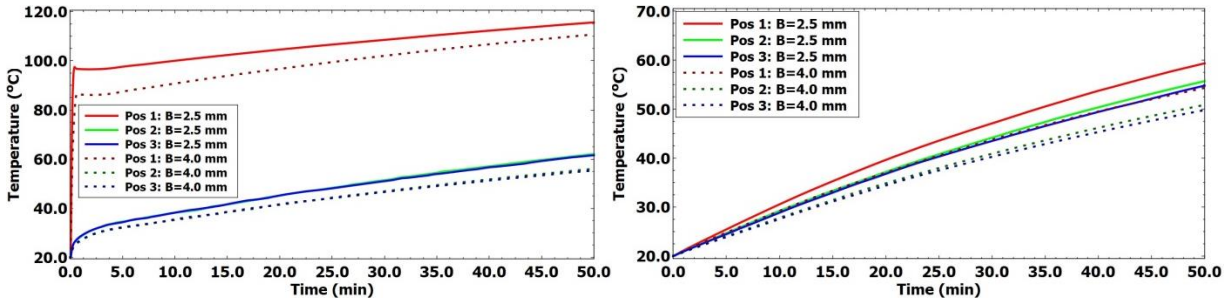

Figure 6: Time responses of the maximum (left) and average temperature (right) in the fluidic volume

As may be noticed, the obtained results imply reaching the highest temperature inside the system (Pos 1), 408.31°C. Likewise, the most promising heat transport processes and where heat diffusion is the fastest is visible for the case where the platform is located inside the chamber (Pos 1), and where the beam is focused. For that position, the average temperature equals 59.36°C after 50 min of irradiation, although the boiling point of water is reached in less than a few minutes. Hence, focusing the laser beam increases the maximum temperature and absorbed power, and it brings the highest heat transportation. Nevertheless, the mean temperature in the chamber still rises for a long time (over 50 min). Therefore, it is indicated to emphasize that 20 min time of illumination is not sufficient to reach the steady-state condition what might be the reason why the side view's temperatures (Figure 4) are not to be compared to the experiments. In order not to falsify and to validate selected Models completely, a few hours of illumination should be performed for further heat diffusion, which requires an additional cooling system for laser operations to preserve the uniform power over the total irradiation time.

Considering thermal processes, it is worth realizing that AuNRs require much less energy in the same time than standard kettles which consume even 1 kW to reach 99°C, which appeals strongly for applying AuNR as a steam generator. Likewise, germs can be inactivated effectively by either thermal ablation, like for Pos 1 case, which provides irreversible modifications in their structures, or reaching the minimum temperature on average in the considered volume in a short time. The obtained results suggest that although the first position (Pos 1) is much more preferred for the microbe's thermal ablation, in the long run, the effectiveness of the process is still time-consuming regardless of the considered location. Therefore, some modifications in the internal fluid are advised, like including high thermal-diffusivity materials. This is the future challenge to optimize the chamber, reflecting the study in this work.

4 CONCLUSIONS

The potential of gold nanorods for thermal processes is highlighted at the designed germicidal chamber where three different AuNR-platform positions have been illuminated. It has been discovered that locations (positions) of the gold nanorod platforms affect the efficient energy conversion. However, the temperature in the designed chamber, when the steady state is reached, is similar for each of the studied positions, although the Pos 1 (inside the chamber) provides the highest temperature increase, and exceeds the rest two locations. The average temperature in the chamber requires long time to reach the satisfied value due to the relatively low diffusivity of water. If the bacteria inactivation processes are taken into account, gold nanorod platforms are indicated to be attached to the transparent wall inside the chamber and be illuminated by a focused beam. Moreover, both presented theoretical models, after slight corrections, can assist to predict and to study the temperature distributions in the entire chamber. Well-designed germicidal chamber will contribute to the pursuit of a sustainable, CO_2-neutral future. Additionally, with heat generated from green technologies, this germicidal chamber has the potential to mitigate CO_2 emissions.

NOMENCLATURE

Roman letters

B	beam size	(m)
C_{abs}	absorption cross-section	(m^2)
C_{ext}	extinction cross-section	(m^2)
C_{sca}	scattering cross-section	(m^2)
c_p	specific heat capacity of a material	($J \cdot kg^{-1} \cdot K^{-1}$)
$\mathbb{D}_{sp}$	spot diameter of gold nanorod sample	(m)
d_{CT}	size of capping agent	(m)
d_l	long diameter of a nanorod (nanorod's length)	(m)
d_s	short diameter of a nanorod (nanorod's size)	(m)
FF	fill factor	(-)
H_0	ambient humidity	(%)
h	heat transfer coefficient	($W \cdot m^{-2} \cdot K^{-4}$)
I_0	incident intensity of light	($W \cdot m^{-2}$)
I_{abs}	absorbed intensity of light	($W \cdot m^{-2}$)
k	thermal conductivity coefficient of a material	($W \cdot m^{-1} \cdot K^{-1}$)
$L_{\mathbb{g}}$	grid (mesh) size	(m)
n_{CT}	refractive index of capping agent	(-)
n_w	refractive index of working medium (here: water)	(-)
P_{abs}	absorbed power	(W)
P_0	incident power of light	(W)
P_{sat}	saturated power as a function of NRs concentration	(W)
p_0	ambient, initial atmospheric pressure	(Pa)
$\mathbb{R}_{Au}$	reflected part of gold	(-)
$\mathbb{R}_{pl}$	reflected part of light for the platform	(-)
$\mathcal{S}_e$	source of energy conversion of gold nanorods	($W \cdot m^{-3}$)
T_0	initial temperature	(K)
$\mathbb{T}$	transmittance	(-)
T	temperature	(K)

Greek letters

$\boldsymbol{\varepsilon_{Au}}$	complex permittivity of gold	(-)
ϵ	emissivity at considered wavelength	(-)
η_{PT}	photothermal efficiency	(-)
η_{TOT}	energy conversion efficiency	(-)
ι_{ph}	phonon (absorbed light) thickness	(m)
λ	incident wavelength (here: 980 nm)	(m)
μ	dynamic viscosity of fluid	($Pa \cdot s$)
ξ	nanorods concentration	(m^{-3})
ρ	density of a material	($kg \cdot m^{-3}$)
φ	mean distance between nanoparticles (here: 20 nm)	(m)

Subscripts, superscripts and abbreviations

o	initial
ABS	absorbance
abs	absorbed
$\boldsymbol{Au}$	gold
CT	capping agent
ext	extinction
e	energy
$\mathbb{g}$	grid

l	long
MAX	maximum (at peak)
PT	photothermal
ph	phonon
pl	platform
p	capacity
sat	saturated
sca	scattering
s	short
w	working fluid

REFERENCES

Bohren, C.F., Huffman, D.R., 1983, Absorption and Scattering of Light by Small Particles, A Wiley-Interscience Publication. John Wiley & Sons, Toronto, 530 p.

El Moutaouakil, L., Boukendil, M., Zrikem, Z. and Abdelabaki, A., 2021, Natural convection and wall radiation in a cubical cavity with different discrete heat source configurations: Geometric parameters effect, Thermal Science and Engineering Progress, vol. 23, p.100874.

Hemati, M., Soosanabadi, M., Ghorashi, T., Ghaffari, H., Vahedi, A., Sabbaghian, E., Rasouli Nejad, Z., Salati, A., Danaei, N., Kokhaei, P., 2021, Thermal inactivation of COVID-19 specimens improves RNA quality and quantity, Journal of Cellular Physiology, 236(7), 4966-72.

Jiang, K., Smith, D.A., Pinchuk, A., 2013, Size-Dependent Photothermal Conversion Efficiency of Plasmonically Heated Gold Nanoparticles, The Journal of Physical Chemistry C, vol. 117, no. 1, p. 27073-27080.

Ji, R., Qin, S., Liu, Y., Jin, L., Yang, C., Meng, X., 2024, Analysis of wettability effects on thermal performance of vapor chamber with a hybrid lattice Boltzmann method, International Journal of Heat and Mass Transfer, vol. 225, p. 125315.

Klein, T.W., Yang, S., Tusty, M.A., Nayak, J.V., Chang, M.T., Bruns, O.T., Bischof, T.S., Valdez, T.A., 2023, Development of a shortwave infrared sinuscope for the detection of cerebrospinal fluid leaks, J Biomed Opt., vol. 28, no. 9, p. 094803.

Lingg, J.G.P., Bischof, T.S., Arús, B.A., Cosco, E.D., Sletten, E.M., Rowlands, C.J., Bruns, O.T., Chmyrov, A., 2023, Shortwave-Infrared Line-Scan Confocal Microscope for Deep Tissue Imaging in Intact Organs, Laser&Photonics Reviews, vol. 17, p. 2300292.

Link, S., El-Sayed, M.A., 2000, Shape and Size Dependence of Radiative, Non-Radiative and Photothermal Properties of Gold Nanocrystals, International Reviews in Physical Chemistry, vol. 19

Liz-Marzán, L., 2020, Colloidal Synthesis of Plasmonic Nanometals, Jenny Stanford Publishing, New York, 910 p.

Li, C., Huang, Y., Jian, Q., Qian, Z., Zou, D., Chen, J., 2024, Experimental and numerical investigation on thermal characteristics of the heat sink integrating 3D vapor chamber heat spreader and liquid cooling fins, Applied Thermal Engineering, vol. 236, B, p. 121609.

Murphy, C. J., Thompson, L. B., Chernak, D. J., Yang, J. A., Sivapalan, S. T., Boulos, S. P., Huang, J., Alkilany, A. M., Sisco, P. N., 2011, Gold Nanorod Crystal Growth: From Seed-Mediated Synthesis to Nanoscale Sculpting., Curr. Opin. Colloid Interface Sci., vol. 16, no. 2, p. 128-134.

Pelton, M., Bryant, G., 2013, Introduction to Metal-Nanoparticle Plasmonics, A Wiley-ScienceWise Publishing Co-Publication. John Wiley & Sons, Hoboken, 275 p.

Peng, I., Jokhio, Alkhaldi, S., Peng C., 2022, Inactivation of SARS-CoV-2 Spike Protein Pseudotyped Virus Infection Using ACE2-Tethered Gold Nanorods under Near-Infrared Laser Irradiation, ACS Appl. Nano Mater., vol. 5, no. 10, p. 15942-15953.

Qu, M., Yu, D., Li, Y., Gao, Z., 2023, Effect of relative chamber width on energy conversion and mechanical characteristics of the offshore OWC device: A numerical study, Energy, vol. 275, p.127372.

Radomski, P., Ziółkowski, P., De Sio, L., Mikielewicz, D., 2021, Computational fluid dynamics simulation of heat transfer from densely packed gold nanoparticles to isotropic media, Archives of Thermodynamics, vol. 42, no. 3, p. 87-114.

Radomski, P., Zaccagnini, F., Ziółkowski, P., Petronella, F., De Sio, L., Mikielewicz, D., 2023a, Heat Transfer of the Multicolor-Laser-Sources-Irradiated Nanoparticles in Reference to Thermal Processes, Proceedings of 36th International Conference on Efficiency, Cost, Optimization, Simulation and Environmental Impact on Energy Systems, ECOS 2023: 356-367

Radomski, P., Ziółkowski, P., Mikielewicz, D., 2023b, Energy conversion in systems-contained laser irradiated metallic nanoparticles - comparison of results from analytical solutions and numerical methods, Acta Mechanica et Automatica, vol. 17, no. 4, p. 540-549.

Radomski, P., Zaccagnini, F., Ziółkowski, P., Petronella, F., De Sio, L., Koulali, A., Mikielewicz, D., 2024, Investigations of Energy Conversion and Surface Effect for Laser-Illuminated Gold Nanorod Platforms, Energies, vol. 17, no. 11, p. 2587.

Siegel, R., Howell, J.R., 1972, Thermal Radiation Heat Transfer, McGraw-Hill Book Company, New York, 816 p.

Shao, L., Majumder, S., Liu, Z., Xu, K., Dai, R., George S., 2022, Light activation of gold nanorods but not gold nanospheres enhance antibacterial effect through photodynamic and photothermal mechanisms, Journal of Photochemistry and Photobiology B: Biology, vol. 231, p. 112450

Wang, F. Zhong, Y., Bruns, O.T., Liang, Y., Dai H., 2024, In vivo NIR-II fluorescence imaging for biology and medicine, Nature Photonics

Wen, J., Smelt, J.P., Vischer, N.O., de Vos, A.L., Setlow, P., Brul, S., 2022, Heat activation and inactivation of bacterial spores: is there an overlap?, Applied and Environmental Microbiology, 88(5), e02324-21.

Xu, P., Peccia, J., Fabian, P., Martyny, J. W., Fennelly, K. P., Hernandez, M., & Miller, S. L. (2003). Efficacy of ultraviolet germicidal irradiation of upper-room air in inactivating airborne bacterial spores and mycobacteria in full-scale studies. Atmospheric Environment, 37(3), 405-419.

Zaccagnini, F., Radomski, P., Sforza, M.L., Ziółkowski, P., Lim, S. I., Jeong, K.U., Mikielewicz, D., Godman, N.P., Evans, D.R., Slagle, J.E., McConney, M.E., De Biase, D., Petronella, F., De Sio, L., 2023,White light thermoplasmonic activated gold nanorod arrays enable the photo-thermal disinfection of medical tools from bacterial contamination, Journal of Materials Chemistry B, vol. 11, no.1, p. 6823- 6836.

Zhan, N., Ding, L., Chai, Y., Wu, J. and Xu, Y., 2019, Experimental study on natural convective heat transfer in a closed cavity, Thermal Science and Engineering Progress, vol. 9, pp.132-141.

Ziółkowski, P., Badur, J., 2018, "A theoretical, numerical and experimental verification of the Reynolds thermal transpiration law," Int. J. Numer. Methods Heat Fluid Flow, vol. 28(1): pp. 64 – 80.

URL 1: https://www.dostal.com.pl/metale-kolorowe-aluminium – a non-standard reference – access date: February 5th, 2024

ACKNOWLEDGEMENTS

This research was funded in whole by National Science Centre in Poland under the project „Shape and displacement optimization of gold nanorods in the killing chamber in order to photothermoablation processes", no UMO-2021/43/D/ST8/02504. For the purpose of Open Access, the author has applied a CC-BY public copyright licence to any Author Accepted Manuscript (AAM) version arising from this submission. This work was performed, in part, at the Center for Integrated Nanotechnologies, an Office of Science User Facility operated for the U.S. Department of Energy (DOE) Office of Science. Los Alamos National Laboratory, an affirmative action equal opportunity employer, is managed by Triad National Security, LLC for the U.S. Department of Energy's NNSA, under contract 89233218CNA000001. María C. Nevárez Martínez was supported by the National Science Centre, Poland, within the scope of the PRELUDIUM-18 project No. 2019/35/N/ST5/00464, entitled "Novel nanomaterials based on titanium composites conjugated with affibody molecules with potential photothermal conversion application". Iuliia Mukha and Luciano De Sio were supported by the Aurum Supporting International Research Team Building, Poland, under research project "Analysis of heat and mass transfer using a dedicated micro-PIV system in a tumor chamber with photothermal-ablated gold nanoparticles". Computations were carried out using the computers of Centre of Informatics Tricity Academic Supercomputer & Network (CI TASK) in Gdansk (Poland). Piotr Radomski is also grateful to the Doctoral School at Gdańsk University of Technology for a scholarship.